Mixed–metal–oxide photocatalysts generated by high–temperature calcination of CaAlFe, hydrocalumite–LDHs prepared from an aluminum salt–cake

Alejandro Jiménez, Raquel Trujillano, Vicente Rives, Miguel Ángel Vicente [*]

GIR–QUESCAT, Departamento de Química Inorgánica, Universidad de Salamanca, E–37008 Salamanca, Spain

ABSTRACT

Solids with photocatalytic properties have been prepared by calcination of hydrocalumite (a sort of layered double hydroxide, LDH) at 750 °C, which had been prepared using an aluminum salt cake as a source. The characterization of the obtained solids was performed by powder X–ray diffraction, FT–infrared spectroscopy, thermal analysis, N_2 adsorption–desorption isotherms at −196 °C and electron microscopy. Different crystalline phases were identified depending on the amount of Fe^{3+} incorporated. The Fe–free photocatalyst showed the best performance under UV light for the photodegradation of ibuprofen.

1. Introduction

Aluminum properties make it an ideal material to be used in various sectors such as military, machinery, aerospace, building or food [1–4]. It is produced by two industrial processes: Primary Aluminum Production (PAP), which is based on the combination of the Bayer and Hall–Héroult processes; and Secondary Aluminum Production (SAP), which is based on one of the most interesting properties of this metal, its recyclable capacity without losing its properties and quality [1–6]. One of the most hazardous and abundant wastes generated during SAP is the so–called Salt cake or Saline Slag [4–8]. Due to its high hazardousness and toxicity for both the environment and living beings, it is considered as a hazardous waste in Europe [9]. Several authors have proposed diverse procedures to recover this waste, either by direct application [10–13] or by submitting it to physicochemical processes that allow the partial recovery of the aluminum present in the salt cake [7] and to use it in the preparation of added–value Al^{3+}–based materials such as alumina [14], zeolites [15–17], or layered double hydroxides (LDHs) [17–23].

The structure of LDHs is derived from that of brucite, $Mg(OH)_2$, by a partial substitution of divalent cations (M(II)) by trivalent ones (M(III)), giving rise to positively charged layers with formula $[M(II)_{(1-x)}M(III)_x(OH)_2]^{x+}$ [24]. This positive charge is balanced by hydrated anions (A^{n-}) in the interlayer space, and therefore the general formula of LDHs can be written as $[M(II)_{1-x}M(III)_x(OH)_2]^{x+}[A_{x/n}]^{n-}\cdot mH_2O$ [24]. A large number of divalent cations (Ni, Co, Cu, Mg, Mn, Ca or Zn) form LDHs with trivalent cations such as Al, Fe, Cr, Mn, V, Y or Ga [24]; even monovalent Li^+ cations can form LDHs with Al^{3+} [25]. When the divalent cation is Ca^{2+}, the trivalent cation is Al^{3+} and the interlayer anion is Cl^-, the resulting LDH is called *Hydrocalumite* ($Ca_2Al(OH)_6Cl\cdot2H_2O$) [24]. Hydrocalumite is a special type of LDH in which the Ca^{2+} and Al^{3+} octahedra are perfectly ordered in the sheet and not randomly distributed as in other LDHs. Moreover, the coordination number of Ca^{2+} is 7, whereas in other LDHs the coordination number of M(II) is 6 [22,24,26–30]. This solid is used such as adsorbent [31–34], antacid [35], ion–exchanger [23,34] and basic heterogeneous catalyst [30,36–39]. Recently, the preparation of hydrocalumite from aluminum salt cake has been reported [22].

Nowadays, the increased consumption of pharmaceuticals and personal care products (PPCPs) has led to these unnatural products belonging to the family of emerging pollutants, to be present in the environment and surface water [33,40–55]. One of the most widely used drugs due to its anti–inflammatory, antipyretic, and analgesic properties is ibuprofen (IBU), whose chemical structure consists of an alkylbenzene ring with a carboxylic acid functional group (Fig.S1) and which pKa is 4.8 [49,56]. Most emerging contaminants, including IBU, cannot be removed from water by classical biological treatments [36–38,43–51, 53,54]; the promising technologies to remove them from water are the so–called Advanced Oxidation Processes (AOPs), especially those based in heterogeneous photocatalysis, a versatile technique based on the use of a photocatalyst and light and that can achieve the degradation and/or

mineralization of pollutants [50–53]. The photocatalyst is a semiconductor material that is activated by light of the appropriate wavelength, generating highly reactive radicals that degrade the pollutant [46,51–53]. Titanium dioxide (TiO_2) is one of the most used photocatalyst [52,58]. However, its relatively low specific surface area, poor surface adsorption rate, limited operation in the UV range and difficulties in its recycling, inevitably restrict its application in some real–life applications. On the other hand, there are many materials with photocatalytic properties such as zinc oxide (ZnO) [51,59], iron (III) oxide (Fe_2O_3) [60], vanadium (V) oxide (V_2O_5) [61], mayenite ($Ca_{12}Al_{14}O_{33}$) [62–64] or more complex materials such as β–$CuGaO_2$ [65] or Bi_2WO_6 [66]. However, many of them lack large–scale application due to their high cost and scarcity. Nevertheless, different photocatalysts such as TiO_2 or ZnO (supported or unsupported) or BiOX (X = Cl or Br) have shown to be effective in the photodegradation of IBU [43,45–48,50,67, 68].

On the other hand, mixed metal oxides (MMOs) can act as supports to disperse the active phase or act as photocatalysts themselves, improving the performance of the overall photocatalytic process [42,52,69]. In this sense, LDHs can be excellent precursors of MMOs through topological transformation by calcination [52,53,59,70,71]. The preparation of bifunctional ZnFe–MMOs from LDH and their photocatalytic application in the degradation of IBU under simulated sunlight has been reported by Di et. al. [68]. Hydrotalcite–type compounds (a family of LDHs similar to hydrocalumite in which M(II) is not Ca^{2+}) and their calcined derivates have been widely used as precursors of MMOs with applications in the removal of emerging contaminants [52,53,59], due to their exceptional properties such as large specific surface area, small band gap, and cheap synthesis. However, to the best of our knowledge, hydrocalumite–type solids (a particular type of LDH) have been scarcely used in contaminant removal [51–53]. Among the studies reported so far, CaAlFe–LDHs have been used for the adsorption of nitrate, chloride and carbonate [72], CaFeAl–MMOs have been used in the heterogeneous catalytic production of biodiesel from soybean oil by transesterification reaction [73], and hydrocalumite–type–compound derivatives have been used in the photocatalytic degradation of 2,4–dichlorophenoxyacetid acid [62]. The presence of transition metals in the starting LDHs improves the photocatalytic properties of both the LDHs and their calcination products [20, 74,75]. The photocatalytic activity of Fe_2O_3 [74–78] and the use of hydrocalumite-type derivative compounds in photocatalysis [26,62] have been reported, but the application of CaAlFe-MMO type solids in photocatalysis, to the best of our knowledge, has hardly been studied.

The aim of this work is to prepare CaAlFe–MMO photocatalysts by calcination at 750 °C of hydrocalumites with general formula $Ca_2Al_{1-m}Fe_m(OH)_6Cl·2 H_2O$, synthesized from an aluminum recycling slag and incorporating variable amounts of Fe^{3+} (m = 0, 0.1, 0.2, 1), and to evaluate their IBU removal capacity in synthetic solutions with a concentration range from 0 to 50 ppm, assessing the possible removal by adsorption and the catalytic photodegradation capacity; studying the influence of the photocatalyst dose on the reaction, and analyzing the recovery and reuse of the catalysts. Although the preparation and characterization of the uncalcined precursors has been previously reported [26], some representative results are here included for the sake of the readers.

2. Experimental

2.1. Materials

The *Salt Cake* was kindly supplied by IDALSA (Ibérica de Aleaciones Ligeras S.L., Spain). NaOH (pharma grade), HCl (pharma grade, 37 %) and $FeCl_3·6H_2O$ (97–102 %) were from Panreac, while $CaCl_2·2H_2O$ (ACS 99–105 %) and Ibuprofen sodium salt (98 %) were supplied by Sigma Aldrich. All the reagents were used as received, without any treatment.

2.2. Preparation of the CaAlFe mixed metal oxides

The methodology recently reported by us [22] to prepare hydrocalumite and Fe^{3+}–doped hydrocalumite was followed [26]. Briefly, the *Salt cake* was ground and washed to obtain a chloride–free solid. It was then sieved through a 0.4 mm light sieve, the fraction smaller than 0.4 mm was extracted with NaOH, and the solution was treated with HCl to remove by precipitation the silicon–containing species [7]. Then the coprecipitation synthesis of the CaAlFe–LDHs was carried out by the addition of $CaCl_2·2H_2O$ and $FeCl_3·6H_2O$ at pH 11 (fixed with NaOH). The precipitate formed was submitted to microwave (MW) treatment in a Milestone Ethos Plus Microwave oven for 2 h at 125 °C, leading to the formation of hydrocalumite–like compounds. Synthetic hydrocalumite samples were named as $CaAl_{1-m}Fe_m$, where *m* represented the amount of Fe^{3+} incorporated into the hydrocalumite–type solid, as the molar fraction of the trivalent cations. In order to evaluate the photocatalytic activity, samples CaAl, $CaAl_{0.90}Fe_{0.10}$, $CaAl_{0.80}Fe_{0.20}$ and CaFe were calcined at 750 °C in air for 2 h using a heating rate of 10 °C/min; this temperature and these samples were selected taking into account the results shown by our previous studies [26,79] for the same precursors, but calcined at 400°C. To identify the calcined solids, the calcination temperature, in Celsius, was added to the name of the samples.

2.3. Characterization techniques

A Siemens D–5000 equipment was used to record the powder X–ray diffraction (PXRD) patterns of the samples (λ = 0.154 nm Cu–Kα radiation, fixed divergence, 5–70° (2θ), scanning rate 2°(2θ)/min, 0.05° steps, 1.5 s/step). The crystalline phases formed were identified by comparison with the JCPDS–International Centre for Diffraction Data [80] (ICDD®).

The FT–IR spectra were recorded in a Perkin–Elmer Spectrum Two instrument with a nominal resolution of 4 cm^{-1} from 4000 to 400 cm^{-1}, using KBr (Merck, grade IR spectroscopy) pressed pellets and averaging 20 scans to improve the signal–to–noise ratio.

Element chemical analyses for Ca, Fe, Al and Si were analyzed out by Inductively Coupled Plasma Optical Emission Spectrometry (ICP–OES) in a Yobin Ivon Ultima II apparatus (Nucleus Research Platform, University of Salamanca, Spain).

The thermogravimetric (TG) curves were recorded in a SDT Q600 apparatus (TA Instruments) at a heating rate of 10 °C/min up to 900 °C and under oxygen (Air Liquide, Spain, 99.999 %) flow (50 mL/min).

The N_2–adsorption–desorption isotherms were recorded at –196 °C using a Micromeritics Gemini VII 2390 T equipment. Prior to analysis, N_2 was flowed through the sample (ca 0.1 g) at 110 °C for 2 h to remove weakly adsorbed species. The specific surface areas were calculated by the Brunauer–Emmet–Teller (BET) [81–83] method and the average pore diameters by the Barrett–Joyner–Halenda (BJH) method [81,84].

Scanning electron microscopy (SEM) images were obtained using a JEOL IT500 Scanning Electron Microscope, at the Nucleus Research Platform (University of Salamanca, Spain).

2.4. Degradation studies

The study of the photocatalytic activity of the synthesized solids was carried out on a MPDS–Basic system from Peschl Ultraviolet, with a PhotoLAB Batch–L reactor and a TQ150–Z0 lamp (power 150 W), integrated in a photonCABINET. Its spectrum is continuous, with the main peaks at 366 nm (radiation flux, Φ 6.4 W) and 313 nm (4.3 W). For this purpose, 750 mL of a solution of IBU sodium salt in distilled water of concentration 50 ppm was introduced into the reaction chamber. This initial IBU concentration was chosen according to previous studies [26, 49]. Different amounts of photocatalyst were added and magnetically stirred in the darkness for 35 min to reach the adsorption–desorption equilibrium, then the UV lamp was turned on. The illumination was cut off and the suspension was allowed to settle down in order to decrease

the losses of photocatalyst as much as possible. Aliquots of liquid were taken and filtered with a Macherey–Nagel CHROMAFIL Xtra PA–20/25 filter of 0.22 μm and analyzed in a Perkin–Elmer LAMBDA 35 ultra-violet–visible spectrophotometer coupled to a computer with UV WIN-LAB 2.85 software, following the evolution in the intensity of the characteristic absorption band of IBU at 222 nm. The reproducibility of the experiments was tested by triplicating some experiments, the difference in the values obtained always being lower than 1 %.

In order to determine the by–products formed during the UV degradation; selected solutions were analyzed after several reaction times by mass spectrometry. The equipment used was an Agilent 1100 HPLC mass spectrometer coupled to an ultraviolet detector and an Agilent Trap XCT mass spectrometer. These analyses were performed at Servicio Central de Análisis Elemental, Cromatografía y Masas (Nucleus Research Platform, University of Salamanca, Spain).

3. Results and discussion

3.1. Extraction of aluminum

A pure aluminum solution was obtained following the extraction conditions previously reported [7,22,26]; the aluminum content in the final extraction solution was 14023 mg/L, while other elements were not found. Then, this pure aluminum solution was used in the coprecipitation synthesis of CaAlFe–LDHs.

3.2. Characterization of the solids

The characteristic peaks of the hydrocalumite–type layered structure (ICDD card 01–072–4773) were found in all X–ray patterns of the samples synthetized (Fig. S2). The high degree of crystallinity is one of the most outstanding peculiarities of hydrocalumite with respect to other LDHs; this is due to the relationship between the ionic radii of the cations composing hydrocalumite: in hydrocalumite the divalent cation is Ca^{2+} which ionic radius (100 pm) [85] is larger than that of Mg^{2+} (72 pm) [85], and in order to fit octahedra with so different sizes of the central cations, it is needed that Ca and Al octahedra are not randomly distributed in the sheets as in hydrotalcite (MgAl–LDH), but are perfectly ordered. On the other hand, if the M(II)/M(III) ratio is set to 2, the difference in radii (r) between the divalent cation (M(II)) and the trivalent one (M(III)) $(r_{M(II)} - r_{M(III)})$ also affects the order of the octahedra in the sheet. In hydrotalcite, this difference varies between 2 pm for MgFe–LDH and 18 pm for ZnAl–LDH, while in hydrocalumite it varies between 18 pm (CaSc–LDH) and 46 pm (CaAl–LDH), i.e., the larger the radius difference, the higher the order of the octahedra in the sheet [24,26,27,86]. Fig. S2 shows that as the Fe^{3+} content in the solid increased, the crystallinity decreased, due to the larger size of Fe^{3+} with respect to Al^{3+} in an octahedral environment. The isomorphic substitution of Al^{3+} by Fe^{3+} implies a decrease in the $r_{M(II)} - r_{M(III)}$ difference and consequently a decrease in the order of the octahedra in the layers, which in turn implies a decrease in the crystallinity [24,27,86]. This observation is similar to that recently reported [26], in which CaAl-Fe–LDHs with different amounts of Fe^{3+} were synthesized and characterized. Other phases were not identified by PXRD.

Fig. S3 shows the thermal behavior of CaAlFe–LDHs, which was described in our previous works [26,79]. In summary, this thermal decomposition in oxygen atmosphere consists of 3 steps: dehydration, dehydroxylation of the layers and decarbonation and/or completion of the dehydroxylation process [26,79]. Taking into account this thermal decomposition process, calcination at 750 ºC – no thermal effects were observed above this temperature– was selected to obtain highly crystalline solids hopefully consisting of mixed metal oxides, to check their photoactivity on IBU photodegradation.

Fig. 1 shows the diffractograms of the samples calcined at 750ºC; formation of crystalline phases was observed in all cases, which shows a great difference with what was reported for the solids calcined at 400 ºC [26], composed of non–crystalline MMOs. Formation of crystalline phases could affect the photochemical behavior of the calcined photocatalysts. However, the formation of one or another crystalline phase depended on the composition of the starting LDH. In the CaAl–750 sample, whose starting LDH is $Ca_2Al(OH)_6Cl \cdot 2H_2O$, the observed phases were mayenite ($Ca_{12}Al_{14}O_{33}$, ICDD card 01–070–2144), calcium hydroxychloride (CaClOH, ICDD card 01–073–1885) and calcium oxide (CaO, ICDD card 01–070–5490), and no amorphous phases were observed, therefore the only phase containing the trivalent cation from LDH was mayenite [26]. Mayenite is a calcium aluminate with a cubic structure and belongs to space group $I\bar{4}3d$ [34,63,87–90]. Mayenite unit cell contains two $Ca_{12}Al_{14}O_{33}$ formulae and consists of a positively charged structure formed by 12 cages and two X ions (X = H^-, O^{2-}, O^-, O_2^-, OH^-, Cl^-, F^- or e^-, all these species are not stable in the atmosphere) occupying two different cages, thus it can be chemically represented as $[Ca_{24}Al_{28}O_{64}]^{4+} \cdot 4X^-$ [63,87–90]. The cages consist of Ca, Al and O ions,

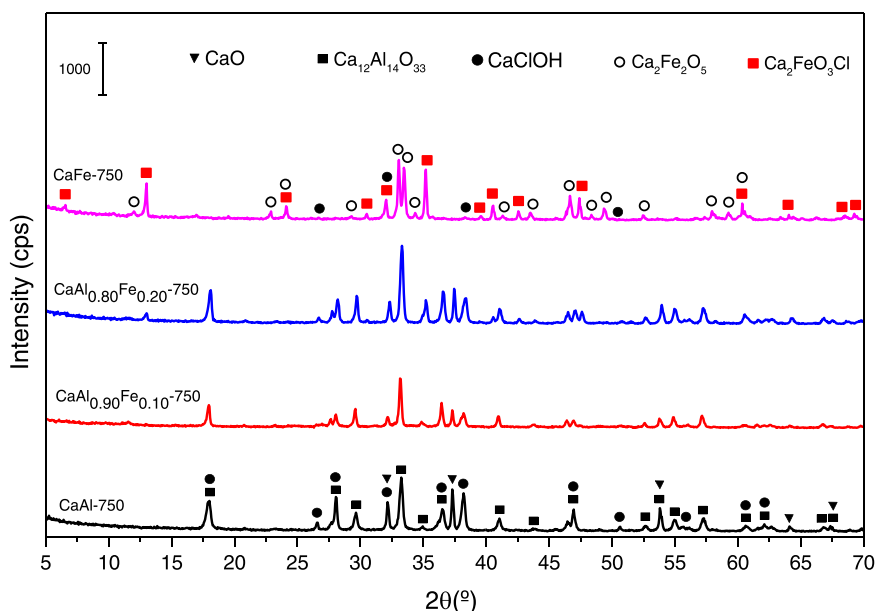**Fig. 1.** X–ray patterns of samples calcined at 750 ºC.

where aluminum occupies octahedral and tetrahedral holes [63,87–90]. When X = O⁻ the solid can act as a generator of reactive oxygen species for chemical reactions and catalytic oxidation [63,87–91], while if X = e⁻ it has application in storage memory devices and as an electron donor in organic synthesis reactions or in noble metal–based heterogeneous catalysis [63,87–91].

When the starting LDH was $Ca_2Fe(OH)_6Cl\cdot2H_2O$, the crystalline phases identified in the solid calcined at 750 °C (CaFe–750) were srebrodolskite ($Ca_2Fe_2O_5$, ICDD card 01–074–3658) and Ca_2FeO_3Cl (ICDD card 01–071–1437). The formation of a mayenite–type phase ($Ca_{12}Fe_{14}O_{33}$), in which the Al^{3+} of the mayenite would be 100 % substituted by Fe^{3+}, was not observed. CaO formation was not observed by PXRD in this sample. However, the presence of CaClOH was observed, although its identification is complex due to the overlapping of the diffraction peaks of the different phases existing in the sample.

Mayenite, calcium hydroxychloride, calcium oxide and Ca_2FeO_3Cl phases were observed in sample $CaAl_{0.90}Fe_{0.10}$–750.

Finally, mayenite, calcium hydroxychloride, calcium oxide and Ca_2FeO_3Cl were identified in the $CaAl_{0.80}Fe_{0.20}$–750 sample. When the fraction of Fe^{3+} cation increased from 0 % to 10 % and from 10 % to 20 % (from m = 0 to m = 0.1 and from m = 0.1 to m = 0.2) and after calcining LDH, it seemed that all Fe^{3+} became part of the phase with formula Ca_2FeO_3Cl. Similarly, aluminum was only incorporated into the mayenite structure in sample CaAl–750, but the amount of Al^{3+} available to form mayenite decreased as m increased, so on increasing m decreased the amount of mayenite formed. These crystalline phases were not identified when the CaAlFe–LDHs samples were calcined at 400 ºC [26].

The FT–IR spectra of the samples calcined at 750 ºC are shown in Fig. 2, all of them being similar to each other. They all showed a broad band in the 3600–3400 cm⁻¹ range, due to the superposition of stretching vibration bands of hydroxyl groups coming from different environments [92]. The band at 1630 cm⁻¹ confirmed the presence of water molecules in the calcined solids. Similarly, the bands at 1412 cm⁻¹ and 877 cm⁻¹ confirmed the presence of carbonate in the samples [39, 92,93], despite the samples had been calcined at a high temperature. Carbonate ions came from the fixation of atmospheric CO_2 due to the basic character of the phases obtained after the calcination process of LDHs. In some samples, the band at 879 cm⁻¹ showed up as a shoulder to the left–hand side of the more intense 832 cm⁻¹ band. The band at 832 cm⁻¹ was not present in the spectrum of sample CaFe–750, therefore

it could be attributed to the Al–OH bond; however, the band assignment in this range of the IR spectrum is complicated due to the overlapping and broadness of the bands. Finally, the bands recorded in the 700–400 cm⁻¹ range were due to M–OH bonds, where M can be Ca^{2+}, Al^{3+} or Fe^{3+} [92].

Fig. 3 shows the nitrogen adsorption–desorption isotherms of the solids calcined at 750 ºC. All isotherms were classified to type II, according to the IUPAC classification criteria [81]. Only the CaFe–750 sample showed a small hysteresis loop, type H3 according to the IUPAC classification criteria [81]. The values of BET specific surface area for the samples uncalcined and calcined at 750 ºC are shown in Table 1. The S_{BET} values increased as the amount of Fe^{3+} did. This agreed with the PXRD observations in Fig. S1, since as the degree of substitution of Al^{3+} by Fe^{3+} increased, the crystallinity of the samples decreased. The calcination process at 750 °C resulted in a further decrease in the S_{BET} of the samples with respect to the starting CaAlFe–LDH and to the solids calcined at 400 °C [26]. Under calcination at 750 °C, much more crystalline solids than the starting LDHs were obtained, and the increase in crystallinity was expected to result in a significant decrease in S_{BET}. On the other hand, as indicated above, hydrocalumite is a special type of LDH in which the Ca^{2+} and Al^{3+} octahedra are perfectly ordered and not randomly distributed as in other LDHs. Moreover, the coordination number of Ca^{2+} is 7, whereas in other LDHs the coordination number of M(II) is 6. This results in an increase of the crystallinity, and consequently a decrease of the S_{BET} of the hydrocalumite-type compounds with respect to other LDHs, with typical S_{BET} values of 7–25 m^2g^{-1} for hydrocalumite [30,35,38]. Furthermore, Souza et al. [38] have calcined CaAl-LDHs at different temperatures, finding that the higher the calcination temperature, the higher the crystallinity of the solid obtained and the lower its S_{BET}, obtaining S_{BET} values for CaAl-LDHs calcined at 600, 700, 800 and 900 ºC of 10.2, 3.9, 3.7 and 1.0 m^2g^{-1}, respectively. The solids calcined at 750 ºC in the present work showed S_{BET} values in agreement with those reported in the literature for this family of solids. On the other hand, the average pore width was in the mesopore range, similar to what was observed for the CaAlFe–LDH solids calcined at 400 ºC [26].

Fig. 4A, B and C show the SEM micrographs of the CaAl–750 sample. Spherical particle aggregates with size between 60 and 80 µm and a rough surface can be observed. In SEM micrographs 4B and 4C these particle aggregates were composed of perfectly defined smaller plate--shaped particles, with sintering of the latter plate–shaped particles to
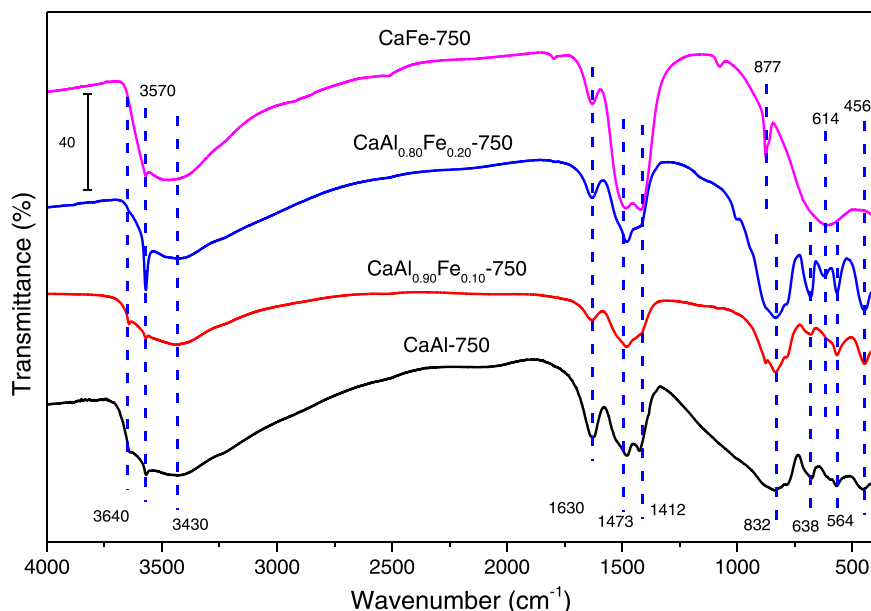

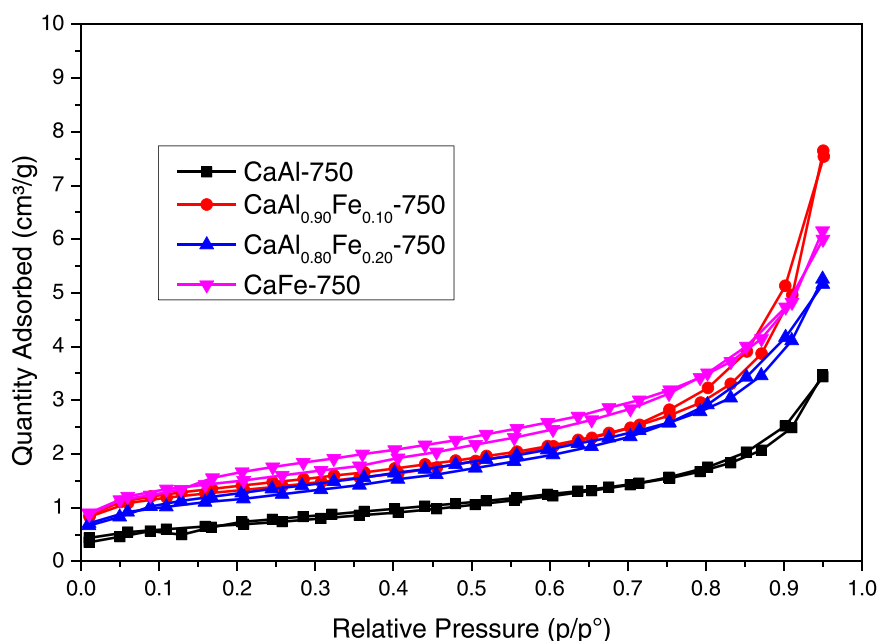**Fig. 2.** FT – IR spectra of the samples calcined at 750 ºC.

Fig. 3. Nitrogen adsorption–desorption isotherms of samples calcined at 750 °C.

Table 1
S_{BET} and average pore diameter of the samples calcined at 750 °C.

Sample	Non–calcined [26]		Calcined at 750 °C	
	S_{BET} (m^2/g)	Average Pore Diameter (nm)	S_{BET} (m^2/g)	Average Pore Diameter (nm)
CaAl	12	8.7	3	8.3
$CaAl_{0.90}Fe_{0.10}$	13	6.2	5	10.8
$CaAl_{0.80}Fe_{0.20}$	20	8.2	7	7.8
CaFe	27	9.3	6	7.6

form the larger aggregates. However, the $CaAl_{0.80}Fe_{0.20}$–750 sample (SEM micrograph 4D) was composed of much smaller (20–40 μm), irregular shaped particle aggregates, compared to the CaAl–750 sample. In micrographs 4E and 4F, these particle aggregates were in turn made up of smaller particles and were much spongier in appearance than the CaAl–750 sample. These smaller particles have a sheet–like shape, but they were very irregular and of a much smaller size than the CaAl–750 sample. Finally, Fig. 4G shows a SEM micrograph of the CaFe–750 sample, where particle aggregates of size close to 100 μm and irregular shape were observed. In the SEM higher magnification micrographs (Fig. 4H and I), aggregates of particles with a totally different aspect and much spongier than the CaAl–750 and $CaAl_{0.80}Fe_{0.20}$–750 samples were observed. In this case, neither regular nor irregular sheet–shaped particles were observed, but particles with a rather spherical appearance that made up the larger aggregates. The spongy aspect of the $CaAl_{0.80}Fe_{0.20}$–750 and especially CaFe–750 samples could justify the fact that these two samples showed S_{BET} values higher than that for the CaAl–750 sample. The degree of sintering between the smaller particles of the CaFe–750 sample also seemed to be higher than that of the other samples.

3.3. Photocatalytic tests

Fig. 5 shows the photodegradation of IBU using the LDHs calcined at 750 °C (CaAl, $CaAl_{0.90}Fe_{0.10}$, $CaAl_{0.80}Fe_{0.20}$, CaFe) as photocatalysts, as well as the result of the photolysis reaction. Removal of the contaminant by adsorption was evaluated for 35 min, and it resulted negligible, similarly to that observed for the same precursors calcined at 400°C [26]. Subsequently, the ultraviolet light lamp was turned on and

photodegradation began. A rapid decrease in the concentration of IBU was observed, with ca. 25 % of the initial concentration remaining in solution 25 min after switching on the ultraviolet light (sixty min since the beginning of the experiment, T_{60}). Up to this point, no significant differences in the photodegradation capacity of the solids were observed, their photocatalytic performance being very similar. However, for longer reaction times, the photocatalyst with the highest performance was the non–containing Fe^{3+} one, CaAl–750, for which only 3 % of the initial concentration of IBU remained after 152 min under irradiation, while for the samples containing Fe^{3+}, the amount remaining after this time was ca. 10 %. Compared to the photocatalysts calcined at 400 °C [26], the CaAlFe–LDHs calcined at 750°C showed a better performance in removing IBU from aqueous samples (Table 2). However, in the absence of any photocatalyst (photolysis reaction), only 21 % of the initial IBU content was eliminated after 152 min [26] and higher than the value reported in other studies, when BiOBr was used as a photocatalyst [43].

The fact that the solid with the best photocatalytic performance was CaAl–750 can be explained by the composition of the crystallographic phases present in this sample, according to the PXRD results, namely, mayenite, CaO and CaClOH. As it was previously indicated, mayenite (a n–type semiconductor [89]) may contain in its structure highly reactive oxygen species, and they would favor the photocatalytic oxidation of IBU. In the other samples, as the amount of Fe^{3+} in the solids increased, the amount of Al^{3+} able to form mayenite with Ca^{2+} decreased, so the mayenite content in the $CaAl_{0.90}Fe_{0.10}$–750 and $CaAl_{0.80}Fe_{0.20}$–750 samples was lower, which may justify the worse photocatalytic performance of these photocatalysts with respect to CaAl–750. Moreover, in the case of these two samples, iron–containing phases ($Ca_2Fe_2O_5$ p–type semiconductor [94]) were formed, and the current results suggested that its photocatalytic activity and/or IBU degradation mechanism could be different – or slower – than that of the CaAl–750 sample (Fig. 6). On the other hand, crystalline mayenite was not detected by PXRD in sample CaFe–750; instead, two phases were identified: Ca_2FeO_3Cl, whose photocatalytic properties, to the best of our knowledge, have not been reported, and $Ca_2Fe_2O_5$, whose photocatalytic activity has been reported for other types of reactions [94], being dependent of the morphology of the $Ca_2Fe_2O_5$ particles, e. g., $Ca_2Fe_2O_5$ nanofibers showed adequate performance in the photocatalytic degradation of Rhodamine B [95].

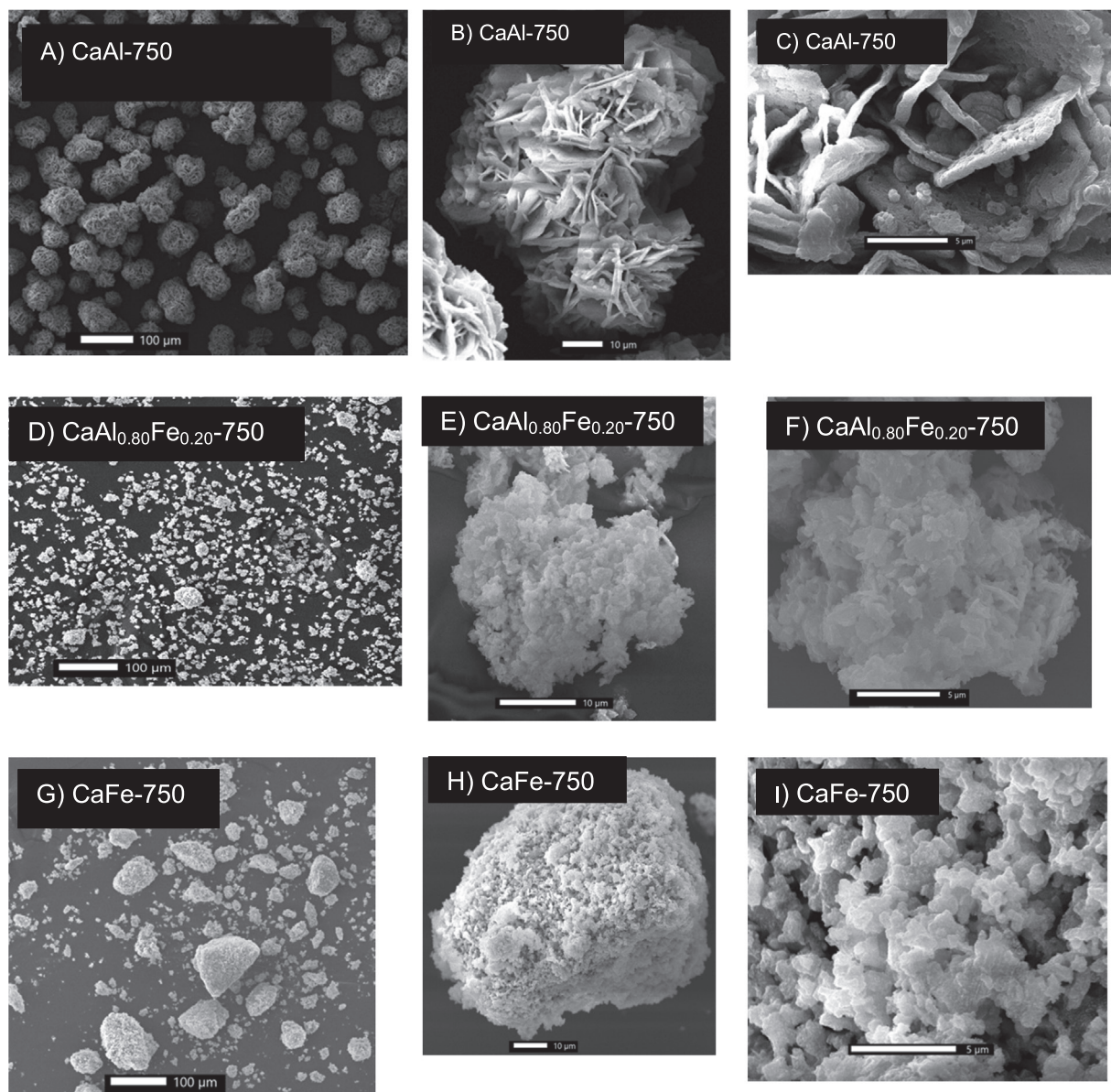Fig. 6 A–D shows the UV–visible spectra of aliquots taken at different

Fig. 4. SEM micrographs of samples calcined at 750º C. Fig. A, B and C show micrographs of CaAl–750 sample. Fig D, E and F belong to CaAl$_{0.80}$Fe$_{0.20}$–750 sample. Fig. G, H and I show SEM micrographs of CaFe–750 sample.

reaction times when each of the catalysts was used. Before switching on the UV lamp, no variation of the characteristic band of IBU at 222 nm was observed [43,96] whereas after switching on the UV lamp, a clear decrease in the intensity of this band was observed, indicating the degradation of IBU was taking place. In all UV–Vis spectra, a band started to appear at 259 nm as the reaction time was increased (Fig. 6 A–D), due to the presence of a degradation by–product of IBU, but it finally disappeared in some cases, indicating that this by–product was also photodegraded, as it was also observed for the solids calcined at 400 ºC [26]. However, the behavior of this band was important, as it varied depending on the photocatalyst used. For the CaAl–750 photocatalyst, it reached its maximum intensity after 7 min under UV irradiation (42 min from the beginning of the experiment) and completely disappeared after 152 min under irradiation, while as the Fe^{3+} content in the photocatalysts increased, this band presented its maximum intensity at longer reaction times; for instance, for the CaAl$_{90}$Fe$_{0.10}$–750 photocatalyst its maximum occurred after 13 min under irradiation and the band did not disappear after 152 min (Fig. 6F); however, for photocatalysts CaAl$_{0.80}$Fe$_{0.20}$–750 and CaFe–750 the band reached its maximum after

15 min under irradiation, being still present even after 152 min under irradiation. Also, as the amount of Fe^{3+} in the photocatalysts increased, the time under irradiation after which the band at 259 nm showed its maximum intensity depended on the photocatalyst used (Fig. 6E). These results seemed to indicate that the Fe^{3+}–containing photocatalysts favored the formation of the degradation by–product characterized by a UV–Vis band at 259 nm and that removal of this by–product required irradiation times longer than 152 min. On the other hand, the CaAl–750 photocatalyst also formed this by–product, characterized by its band at 259 nm, but a priori the amount formed must be lower than that formed in the case of the Fe^{3+}–containing photocatalysts and finally this by--product was completely degraded, as the band at 259 nm did not appear after 152 min under UV irradiation (Fig. 6F). The main degradation metabolites reported under treatment of IBU by AOPs chemical methods in aqueous solutions are included in Table 3 [26,43,45,57,67,96–99].

The final aliquots corresponding to an irradiation time of 152 min (T$_{187}$) were analyzed by HPLC–MS, which showed the presence of only two compounds: C$_{13}$H$_{18}$O$_2$, IBU, and another compound of formula C$_{13}$H$_{18}$O$_4$. The latter compound appeared to be a hydroxylated
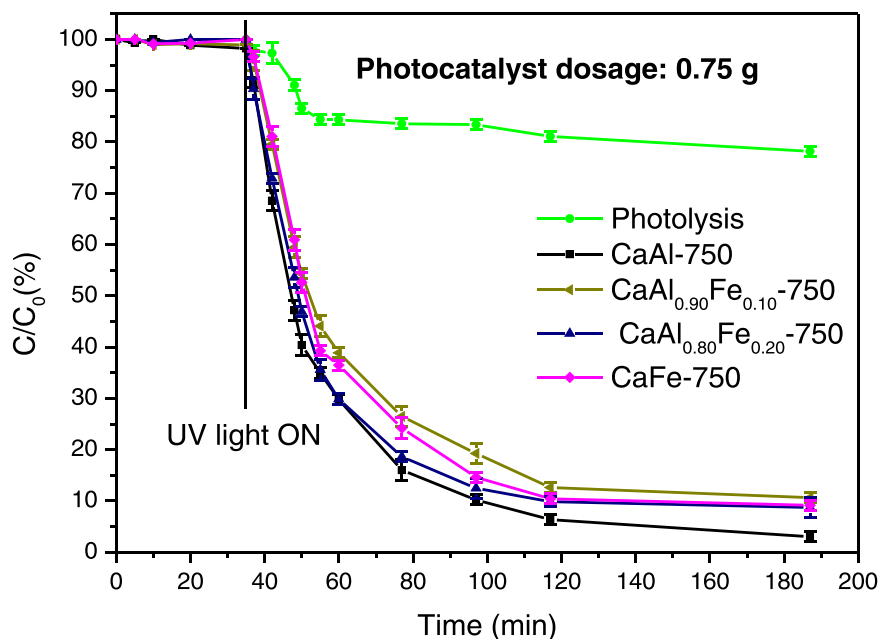
Fig. 5. IBU photodegradation using the samples calcined at 750ºC (photolysis is included for comparison).

Table 2
Percentage of IBU removed depending on the calcination temperature of the CaAlFe–LDHs after 152 min of irradiation (values for the photocatalysts calcined at 400 ºC are taken from [26]).

Photocatalyst	Calcination temperature (ºC)	
	400 ºC	750 ºC
CaAl	95.3	97.0
CaAl$_{0.90}$Fe$_{0.10}$	87.0	90
CaAl$_{0.80}$Fe$_{0.20}$	85.0	88.5
CaFe	83.0	87.5

derivative of IBU, which may be formed through a mechanism involving OH• radicals [26]. IBU and the compound of formula $C_{13}H_{18}O_4$ were detected by HPLC–MS in all aliquots at which the band at 259 nm reached its maximum intensity. The intermediate metabolites characteristic of IBU photodegradation shown in Table 3 were not identified in any of the samples analyzed by HPLC–MS. Thus, it can be concluded that after 152 min of irradiation, only 3 % of IBU still remained in the aqueous solutions and that the photodegradation of IBU using photocatalysts prepared by calcination of CaAlFe–LDHs at 750 °C seemed to proceed through a dihydroxylated intermediate of IBU. This dihydroxylated intermediate was detected in all the final solutions, in a very small amount for photocatalyst CaAl–750 and in higher amounts for the Fe^{3+}–containing photocatalysts. It can be tentatively proposed that the Fe^{3+}–containing photocatalysts require longer irradiation times than CaAl–750 photocatalyst to photodegrade the dihydroxylated intermediate of IBU photodegradation.

As indicated above, mayenite can act as a generator or reactive oxygen species for chemical reactions and catalytic oxidation [59,80–84]. A possible mechanism through which photocatalytic oxidation of IBU could take place using CaAl–750 as a photocatalyst is shown in Scheme 1. The reaction would start with the generation of OH• species, which in a second step would attack the carbonyl group at the alpha carbon, a benzyl carbon, so that forming a highly stabilized tertiary radical, as shown in step 3, and a water molecule. The attack in this position would be favored by the basic pH of the medium generated by the CaAl–750 photocatalyst, as the hydrogen atom located at position alpha to a carbonyl has a certain acidic character. The interaction of the radical generated in step 3 with a water molecule –steps 4 and 5– leads to

formation of a hydroxylated derivative of IBU (step 6). From this point on, the reaction can proceed through two different pathways (a and b in Scheme 1) to form the dihydroxylated IBU derivatives. In the case of pathway *a*, a tertiary radical shown in steps 7*a* and 8*a* is formed, which finally interacts with a water molecule (steps 9*a*, 10*a* and 11*a*) to form the compound shown in 12*a*. On the other hand, in the case of pathway *b*, a benzyl radical is formed again (steps 7*b* and 8*b*), which then interacts with a water molecule (steps 9*b*, 10*b* and 11*b*) to form the dihydroxylated derivative shown in 12*b*. This proposal is feasible for justifying the formation of the dihydroxylated derivatives with formula $C_{13}H_{18}O_4$ detected by HPLC–MS, very scarcely reported in the literature [37,92]. However, further studies would be required in order to understand the mechanism of the photodegradation of IBU using this type of photocatalysts since, according to our knowledge, only Sánchez–Cantú et al. [58] have used hydrocalumite–derived catalysts (without Fe) in the elimination of an emerging pollutant, namely 2, 4–dichlorophenoxyacetic acid. Although these pathways suggested interesting mechanisms for the degradation of IBU, unfortunately its complete mineralization could not be determined.

3.4. Photocatalyst dosage

In order to determine the optimum amount of photocatalyst in the photodegradation experiments, the best performing photocatalyst CaAl–750 was selected (750 mL of 50 ppm IBU solutions were always used). Fig. 7 shows the removal of IBU using different doses of this photocatalyst CaAl–750. Adsorption was initially evaluated for 35 min and the sample was then irradiated with UV light for a total of 152 min Fig. 7 shows that at low doses of photocatalyst (0.25 g and 0.50 g) the performance in the removal of IBU was slightly lower than when higher amounts of photocatalyst were used. On the other hand, when higher doses of photocatalyst (0.75 g, 1.00 g and 2.00 g) were used, the performance in the elimination of IBU was slightly higher for short irradiation times than that obtained when lower doses of photocatalyst were used. This could be due to the fact that increasing the photocatalyst dose increased the number of active centers. However, the performance in the removal of IBU when using doses of 1.00 and 2.00 g for 25 min under irradiation (T_{60}) resembled the performance when using low doses of photocatalyst (0.25 g and 0.50 g), which may indicate that at doses higher than 0.75 g not all solid particles were exposed to the UV light, as

some particles were obscured by others. However, for the dose of 0.75 g the performance increased, being this the dose with the best performance in the photodegradation of IBU. Therefore, the optimum dose of photocatalyst in 750 mL of 50 ppm IBU solution is 0.25 g, or a photocatalyst mass to solution volume ratio of 3.33×10^{-4} g/mL.

3.5. Influence of pH

In the case of photolysis, the pH remained almost constant and close to a value of 6.4 throughout the experiment, a value slightly higher than that of distilled water exposed to atmospheric CO_2 (5.8). However, when photocatalyst CaAl–750 was used, the initial pH was 6.4 and it rose immediately to a value of 11.5 after 5 min. This increase in pH could be attributed to the presence of the photocatalyst. This increase in pH and the high solubility of the photocatalyst at acidic pH made the determination of the pH of the zero-charge point (pHPCZ) practically impossible. According to PXRD, the photocatalyst was made up of three phases: Mayenite, CaO and CaClOH, all of them with an alkaline

character. On the other hand, CaO could react with water to form Ca $(OH)_2$, releasing OH^- ions into the medium, which could also justify the observed increase in pH. After this initial increase, the pH remained almost constant during the experiment, at values between 11.35 and 11.75. These pH changes should not significantly affect the IBU –related species present in solution in the different experiments, as IBU pK_a is 4.8 [49,56].

Taking into account the pH increase produced by the addition of photocatalyst CaAl–750, it was decided to study its influence on the photodegradation of IBU. For this purpose, a photolysis experiment was carried out by adding, prior to the experiment, the appropriate amount of NaOH to reach pH = 11.5. Fig. 8B shows the photolysis at natural pH and at pH 11.5; the increase in pH favored removal of IBU, rising from 22 % to 50 %. Therefore, it can be concluded that IBU was more easily eliminated by photolysis under basic pH conditions, similarly to that reported by Li et al. [56]. In addition, the photocatalytic activity of photocatalyst CaAl–750 was evaluated by previously adjusting the pH to 11.5 with NaOH (thus, the solubilization of the solid should be
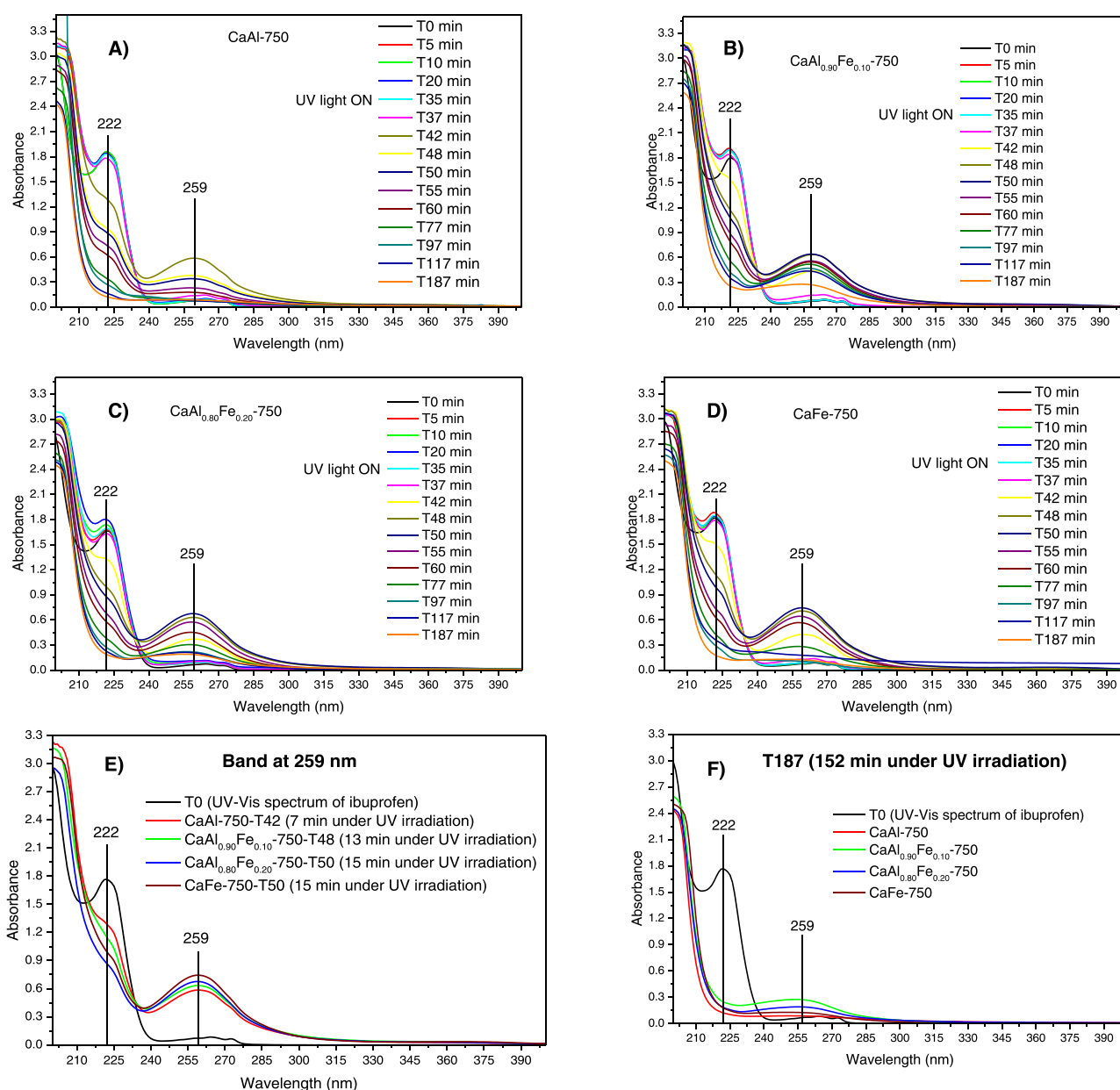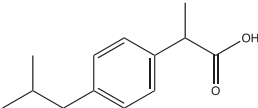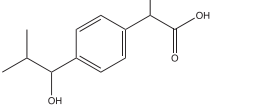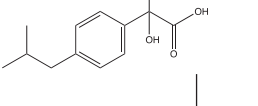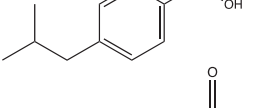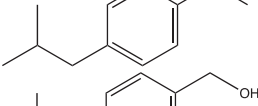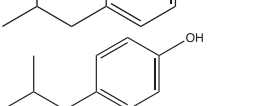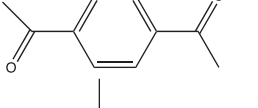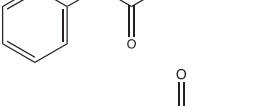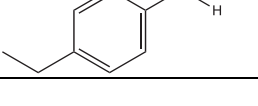

Fig. 6. Ultraviolet–visible spectra of samples taken at different reaction times when different photocatalysts were used: (A) CaAl–750; (B) CaAl$_{0.90}$Fe$_{0.10}$–750; (C) CaAl$_{0.80}$Fe$_{0.20}$–750; (D) CaFe–750. (E) UV–vis spectrum of the aliquot at which the absorbance maximum of the band at 259 occurs, and UV–Vis spectra of IBU. (F) UV–Vis spectra of IBU and aliquot at T$_{187}$.

Table 3

Main intermediates of IBU degradation.

Name	Formula	Molecular structure	MW	*m/z* (major ions)	Reference
2–(4–isobutylphenyl)propionic acid	$C_{13}H_{18}O_2$		206	206, 163, 161 (100 %), 119, 117, 107, 91	[45,49,56,99]
2–[4–[4–(1–hydroxy–2–methylpropyl)phenyl] propanoic acid	$C_{13}H_{18}O_3$		222	177(100 %), 159, 59	[45,98,99]
1–(4–isobutylphenyl)–1–ethanol	$C_{12}H_{18}O$		178	163 (100 %), 57, 43	[45,67,98]
4–Isobutylacetophenone	$C_{12}H_{16}O$		176	176, 161 (100 %), 134, 91, 43	[43,45,67,96,99]
4–isobutylphenylcarbinol	$C_{11}H_{15}O$		163	149 (100 %), 147, 133, 106, 105, 91, 77	[43]
4–isobutylphenol	$C_{10}H_{14}O$		150	150, 107 (100 %), 77, 39	[96,97]
4–Acetylacetophenone	$C_{10}H_{10}O_2$		162	162, 148, 147 (100 %), 119, 43, 91	[43]
Hydratropic acid	$C_9H_{10}O_2$		150	150, 105 (100 %), 77	[97]
4–ethylbenzaldehyde	$C_9H_{10}O$		134	134 (100 %), 133, 119, 105, 91, 79, 77, 51	[97]

minimized, and more amount of solid photocatalyst would be available). In this case, no significant differences were found in the photo-degradation capacity of CaAl–750 as a function of pH (Fig. 9B), showing similar values both at natural pH and at pH 11.5. Therefore, it can be concluded that in the presence of the photocatalyst, the increase in pH did not produce an increase in the removal of IBU.

3.6. Recycling studies

Reuse studies were carried out on photocatalyst CaAl–750. It was separated from the IBU solution by centrifugation after the end of the photocatalysis experiment, washed repeatedly with cold water, dried at 70 °C overnight and characterized by PXRD. Fig. 9A shows the PXRD diagram of CaAl–750 photocatalyst after one photocatalytic cycle. The layered structure of the starting LDH was recovered, i.e., the hydro-calumite mineralogical phase (Ca$_2$Al(OH)$_6$Cl·2H$_2$O) was formed, what was in agreement with the so–called "memory effect" reported for reconstruction of calcined LDHs in aqueous solutions [24,100–104]. The "memory effect", one of the most attractive properties of LDHs, consists in that after calcining the LDH at a temperature at which the collapse of the layered structure occurs to give rise to a mixture of mostly

amorphous oxides, the further contact of these calcined solid with an aqueous solution containing anions capable of entering into the inter-layer space of the LDH allows to recover the layered structure of the LDH. In the present case, it was very remarkable that the memory effect applied even for a solid calcined at 750 °C. On the other hand, such a reconstruction interfered with reuse of the catalyst, suggesting that the solid should be re–calcined after each catalytic cycle. In addition to the hydrocalumite phase, formation of calcite (CaCO$_3$) in the used solid was also observed, which may be caused by the fixation in the alkaline so-lutions of atmospheric CO$_2$ or even of CO$_2$ generated by mineralization of IBU. In the present case, the used solid was re–calcined at 750 °C. The PXRD diagram of this re–calcined solid (Fig. 9) showed that mayenite and CaO phases were formed again, while CaClOH was not identified. This re–calcined solid was used in the photodegradation of IBU, showing good photocatalytic activity, although slightly lower than that of the first cycle (Fig. 9).

4. Conclusions

Solids with photocatalytic properties in IBU photodegradation have been synthesized by calcination at 750 °C of CaAlFe–LDHs which had
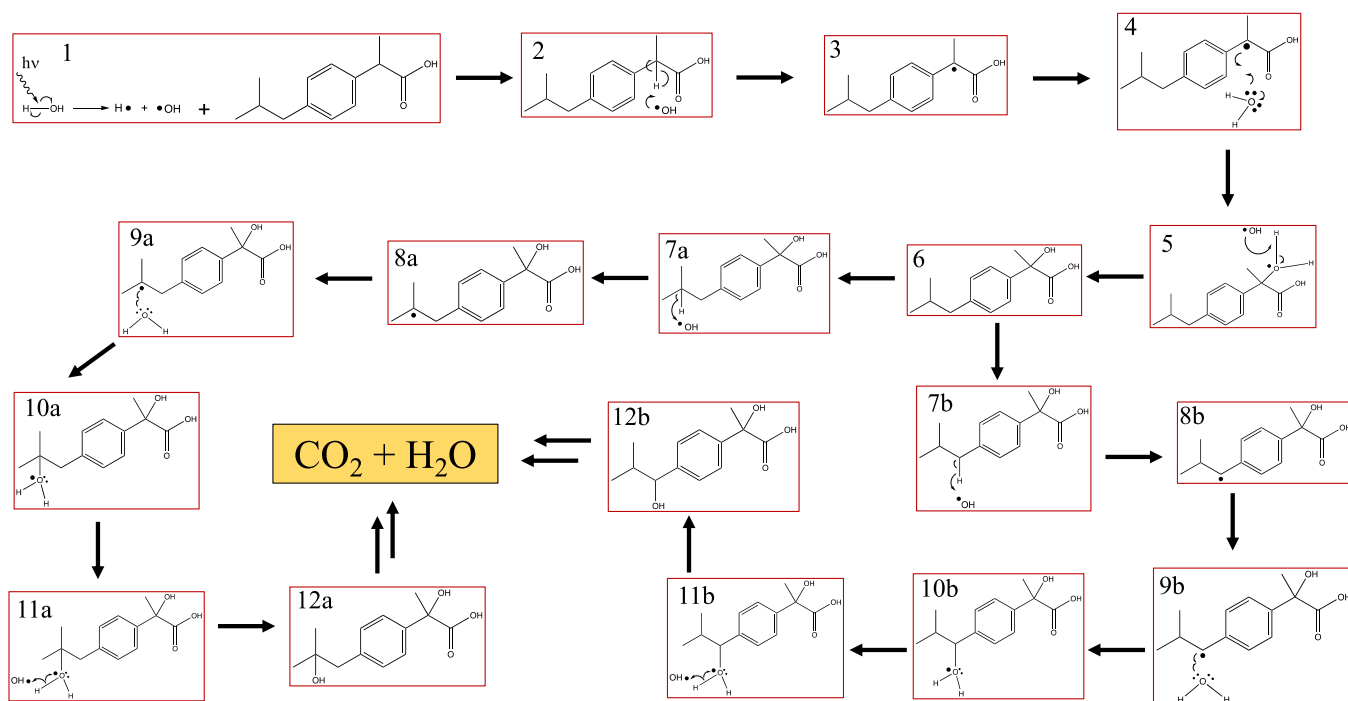
Scheme 1. Mechanism proposal for the formation of the dehydroxylated derivatives of IBU.
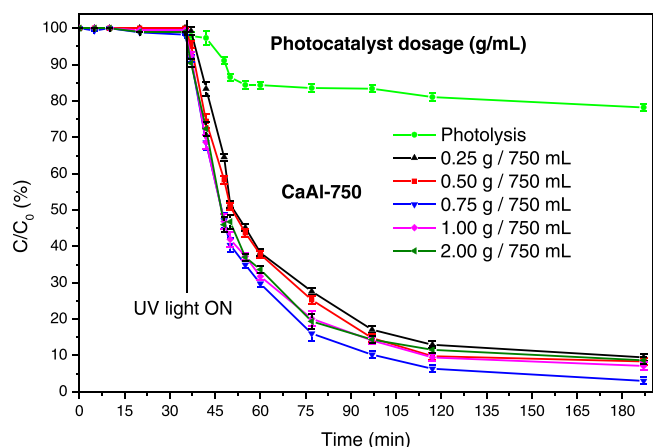

Fig. 7. Photodegradation of IBU when different dosages of photocatalyst CaAl–750 were used.

been synthesized using *salt cake* as a source of aluminum. The presence of Fe^{3+} affected the crystallographic phases formed by calcination of the LDHs at 750 °C, so that when there was no Fe^{3+} the crystallographic phases identified were mayenite, CaO and CaClOH, whereas when Fe^{3+} was present in the starting LDH, the isomorphic substitution of Al^{3+} by Fe^{3+} did not occur to form a solid of formula $Ca_{12}Fe_{14}O_{33}$ similar to mayenite; instead, other phases were formed in addition to mayenite, namely and srebrodolskite ($Ca_2Fe_2O_5$). When the starting LDH did not contain Al^{3+}, the formation of mayenite was not detected, while if it contained Fe^{3+}, formation of CaO was not observed. All the prepared solids showed good photocatalytic performance in the removal of IBU from aqueous solutions; the photocatalyst with the best performance was CaAl–750, which did not contain Fe^{3+}. The degree of photo-degradation of IBU, as well as the degradation metabolites present in the final solutions, were affected by the presence of Fe^{3+} in the solids. The only by–product identified was a dihydroxylated derivative of IBU ($C_{13}H_{18}O_4$), which for CaAl–750 reaches its maximum formation after 7 min under irradiation and was finally almost totally degraded at

longer photoreaction times, while in the photocatalysts containing Fe^{3+} the maximum formation of this by–product was reached at longer irradiation times (approx. 15 min) and was even identified by UV–Vis spectroscopy in the final solution after 152 min under irradiation.

The dose of photocatalyst was optimized, resulting in a photocatalyst/solution volume ratio of 3.33×10^{-4} g/mL (concentration of IBU being 50 ppm). The influence of pH on the elimination of IBU by photocatalytic degradation has also been studied, observing that in the absence of photocatalyst, the percentage eliminated by photolysis was approximately twice at pH 11.5 than at pH 6.4. However, pH had a non–appreciable effect when using photocatalyst CaAl–750. Finally, the reusability of the CaAl–750 photocatalyst was studied and it was found to be active after at least two cycles. During the photocatalytic experiments, the photocatalyst recovered the layered structure of the starting hydrocalumite (memory effect), which made necessary to calcine it again before reusing it, showing almost the same photoactivity in the second cycle.

CRediT authorship contribution statement

All the authors have participated in all the parts of this work. This work belongs to the Ph. D. Thesis of AJ, supervised by VR and MAV; while RT belongs to the Research Group and collaborated in all the steps of the work. By this reason, AJ was the author most intensely involved in the experimental part of the work and in the elaboration of the results, while RT, VR and MAV mostly participated in the design of the work, the revision and validation of the results, and obtaining of financing. All the authors know and approve the submission of this manuscript.

Declaration of Competing Interest

The authors declare that they have no known competing financial interests or personal relationships that could have appeared to influence the work reported in this paper.

Data Availability

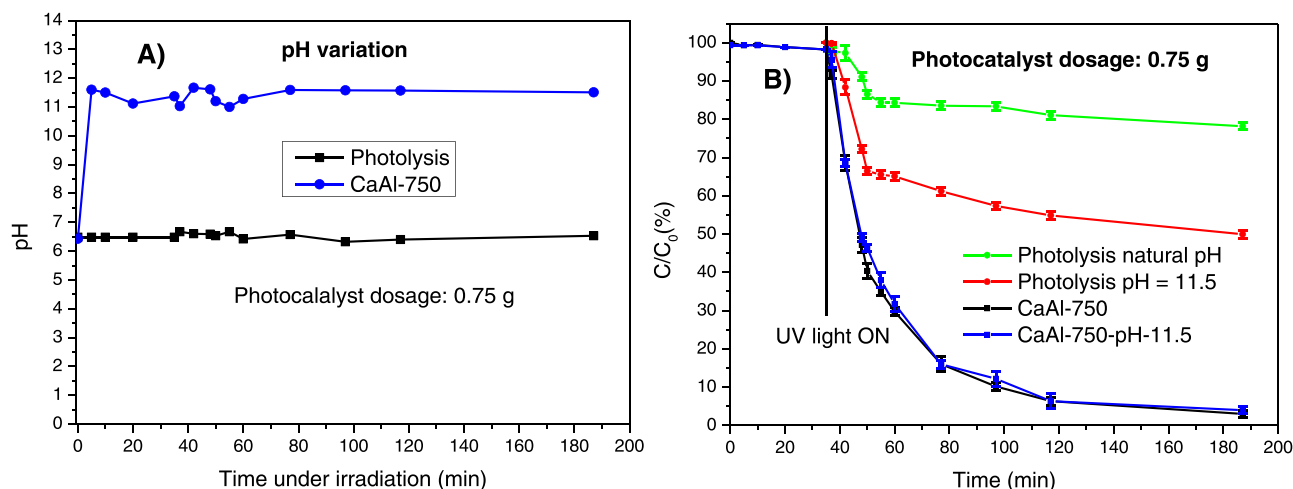No data was used for the research described in the article.

Fig. 8. Influence of pH on IBU degradation. (A) pH variation along the experiment. (B) photodegradation experiments of photolysis and CaAl–750 photocatalyst at natural pH and pH = 11.5.
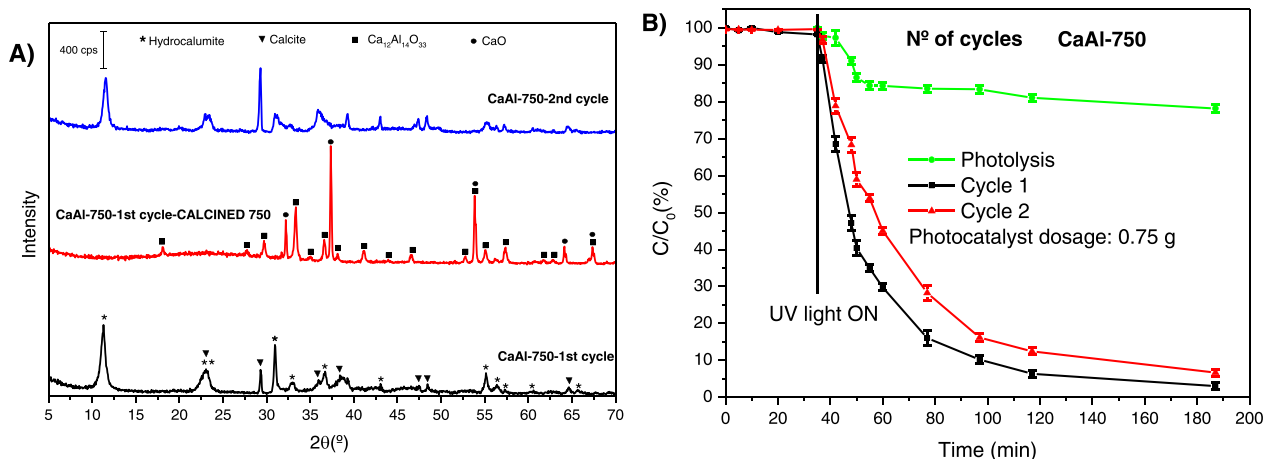

Fig. 9. Recycling studies. Fig. 9A shows the diffractograms of the CaAl–750 photocatalyst after being used and subsequently calcined at 750 ºC. Fig. 9B shows the photocatalytic efficiency of the solid CaAl–750 in 2 cycles.

Acknowledgements

Appendix A. Supporting information

Supplementary data associated with this article can be found in the online version at doi:10.1016/j.cattod.2023.01.015.

References

[1] L. He, L. Shi, Q. Huang, W. Hayat, Z. Shang, T. Ma, M. Wang, W. Yao, H. Huang, R. Chen, Extraction of alumina from aluminum dross by a non-hazardous alkaline sintering process: Dissolution kinetics of alumina and silica from calcined materials, Sci. Total Environ. 777 (2021), 146123, https://doi.org/10.1016/j.scitotenv.2021.146123.

[2] P.E. Tsakiridis, Aluminium salt slag characterization and utilization - a review, J. Hazard. Mater. 217–218 (2012) 1–10, https://doi.org/10.1016/j.jhazmat.2012.03.052.

[3] P.E. Tsakiridis, P. Oustadakis, K. Moustakas, S.L. Agatzini, Cyclones and fabric filters dusts from secondary aluminium flue gases: a characterization and leaching study, Int. J. Environ. Sci. Technol. 13 (2016) 1793–1802, https://doi.org/10.1007/s13762-016-1014-3.

[4] M. Mahinroosta, A. Allahverdi, Hazardous aluminum dross characterization and recycling strategies: a critical review, J. Environ. Manag. 223 (2018) 452–468, https://doi.org/10.1016/j.jenvman.2018.06.068.

[5] A. Meshram, K.K. Singh, Recovery of valuable products from hazardous aluminum dross: a review, Resour. Conserv. Recycl. 130 (2018) 95–108, https://doi.org/10.1016/j.resconrec.2017.11.026.

[6] A. Gil, Management of the salt cake from secondary aluminum fusion processes, Ind. Eng. Chem. Res. 44 (2005) 8852–8857, https://doi.org/10.1021/ie050835o.

[7] A. Jiménez, V. Rives, M.A. Vicente, A. Gil, A comparative study of acid and alkaline aluminum extraction valorization procedure for aluminum saline slags, J. Environ. Chem. Eng. 10 (2022), 107546, https://doi.org/10.1016/j.jece.2022.107546.

[8] M. Lukita, Z. Abidin, E. Riani, A. Ismail, Utilization of hazardous waste of black dross aluminum: processing and application-a review, J. Degrad. Min. Lands Manag. 9 (2022) 3265–3271, https://doi.org/10.15243/jdmlm.2022.092.3265.

[9] Directive 2010/75/EU, 2022.

[10] A. López-Delgado, J.I. Robla, I. Padilla, S. López-Andrés, M. Romero, Zero-waste process for the transformation of a hazardous aluminum waste into a raw material to obtain zeolites, J. Clean. Prod. 255 (2020) 1200178, https://doi.org/10.1016/j.jclepro.2020.120178.

[11] A. Gil, E. Arrieta, M.Á. Vicente, S.A. Korili, Application of industrial wastes from chemically treated aluminum saline slags as adsorbents, ACS Omega 3 (2018) 18275–18284, https://doi.org/10.1021/acsomega.8b02397.

[12] A. Gil, S.A. Korili, Management and valorization of aluminum saline slags: current status and future trends, Chem. Eng. J. 289 (2016) 74–84, https://doi.org/10.1016/j.cej.2015.12.069.

[13] A. Gil, S. Albeniz, S.A. Korili, Valorization of the saline slags generated during secondary aluminium melting processes as adsorbents for the removal of heavy metal ions from aqueous solutions, Chem. Eng. J. 251 (2014) 43–50, https://doi.org/10.1016/j.cej.2014.04.056.

[14] B.R. Das, B. Dash, B.C. Tripathy, I.N. Bhattacharya, S.C. Das, Production of η-alumina from waste aluminium dross, Miner. Eng. 20 (2007) 252–258, https://doi.org/10.1016/j.mineng.2006.09.002.

[15] M. Yoldi, E.G. Fuentes-Ordoñez, S.A. Korili, A. Gil, Zeolite synthesis from industrial wastes, Microporous Mesoporous Mater. 287 (2019) 183–191, https://doi.org/10.1016/j.micromeso.2019.06.009.

[16] A. Jiménez, A. Misol, Á. Morato, V. Rives, M.A. Vicente, A. Gil, Synthesis of pollucite and analcime zeolites by recovering aluminum from a saline slag, J. Clean. Prod. 297 (2021), 126667, https://doi.org/10.1016/j.jclepro.2021.126667.

[17] A. López-Delgado, O. Rodríguez, I. Padilla, R. Galindo, S. López-Andrés, Industrial aluminum hazardous waste as a new raw material for zeolite synthesis, WIT Trans. Ecol. Environ. 180 (2014) 273–282, https://doi.org/10.2495/WM140231.

[18] A. Gil, E. Arrieta, M.A. Vicente, S.A. Korili, Synthesis and CO2 adsorption properties of hydrotalcite-like compounds prepared from aluminum saline slag wastes, Chem. Eng. J. 334 (2018) 1341–1350, https://doi.org/10.1016/j.cej.2017.11.100.

[19] L. Santamaría, M. López-Aizpún, M. García-Padial, M.A. Vicente, S.A. Korili, A. Gil, Zn-Ti-Al layered double hydroxides synthesized from aluminum saline slag wastes as efficient drug adsorbents, Appl. Clay Sci. 187 (2020) 105486, https://doi.org/10.1016/j.clay.2020.105486.

[20] L. Santamaría, M.A. Vicente, S.A. Korili, A. Gil, Saline slag waste as an aluminum source for the synthesis of Zn–Al–Fe–Ti layered double-hydroxides as catalysts for the photodegradation of emerging contaminants, J. Alloy. Compd. 843 (2020), 156007, https://doi.org/10.1016/j.jallcom.2020.156007.

[21] L. Santamaría, L. Oliveira García, E.H. de Faria, K.J. Ciuffi, M.A. Vicente, S.A. Korili, A. Gil, M(II)-Al-Fe layered double hydroxides synthesized from aluminum saline slag wastes and catalytic performance on cyclooctene oxidation, Miner. Eng. 180 (2022), 107516, https://doi.org/10.1016/j.mineng.2022.107516.

[22] A. Jiménez, A. Misol, Á. Morato, V. Rives, M.A. Vicente, A. Gil, Optimization of hydrocalumite preparation under microwave irradiation for recovering aluminium from a saline slag, Appl. Clay Sci. 212 (2021), 106217, https://doi.org/10.1016/j.clay.2021.106217.

[23] N. Murayama, I. Maekawa, H. Ushiro, T. Miyoshi, J. Shibata, M. Valix, Synthesis of various layered double hydroxides using aluminum dross generated in aluminum recycling process, Int. J. Miner. Process 110–111 (2012) 46–52, https://doi.org/10.1016/j.minpro.2012.03.011.

[24] V. Rives, Layered Double Hydroxides, Nova Science Publishers, Inc, New York, 2001.

[25] J.P. Thiel, C.K. Chiang, K.R. Poeppelmeier, Structure of LiAl2(OH)7·2H2O, Chem. Mater. 2 (1993) 297–304.

[26] A. Jiménez, M. Valverde, A. Misol, R. Trujillano, A. Gil, M.Á. Vicente, Preparation of Ca2Al1−mFem(OH)6Cl 2H2O-doped hydrocalumites and application of their derived mixed oxides in the photodegradation of ibuprofen, ChemEngineering 6 (2022), https://doi.org/10.3390/chemengineering6040064.

[27] I. Rousselot, C. Taviot-Guého, F. Leroux, P. Léone, P. Palvadeau, J.P. Besse, Insights on the structural chemistry of hydrocalumite and hydrotalcite-like materials: Investigation of the series Ca2M3+(OH)6Cl·2H2O (M3+: Al3+, Ga3+, Fe3+, and Sc3+) by X-ray powder diffraction, J. Solid State Chem. 167 (2002) 137–144, https://doi.org/10.1006/jssc.2002.9635.

[28] E. Pérez-Barrado, M.C. Pujol, M. Aguiló, Y. Cesteros, F. Díaz, J. Pallarès, L.F. Marsal, P. Salagre, Fast aging treatment for the synthesis of hydrocalumites using microwaves, Appl. Clay Sci. 80–81 (2013) 313–319, https://doi.org/10.1016/j.clay.2013.05.006.

[29] J. Granados-Reyes, P. Salagre, Y. Cesteros, Effect of microwaves, ultrasounds and interlayer anion on the hydrocalumites synthesis, Microporous Mesoporous Mater. 199 (2014) 117–124, https://doi.org/10.1016/j.micromeso.2014.08.004.

[30] J. Granados-Reyes, P. Salagre, Y. Cesteros, Effect of the preparation conditions on the catalytic activity of calcined Ca/Al-layered double hydroxides for the synthesis of glycerol carbonate, Appl. Catal. A Gen. 536 (2017) 9–17, https://doi.org/10.1016/j.apcata.2017.02.013.

[31] Y. Takaki, X. Qiu, T. Hirajima, K. Sasaki, Removal mechanism of arsenate by bimetallic and trimetallic hydrocalumites depending on arsenate concentration, Appl. Clay Sci. 134 (2016) 26–33, https://doi.org/10.1016/j.clay.2016.05.010.

[32] M. Hossein Beyki, M. Mohammadirad, F. Shemirani, A.A. Saboury, Magnetic cellulose ionomer/layered double hydroxide: an efficient anion exchange platform with enhanced diclofenac adsorption property, Carbohydr. Polym. 157 (2017) 438–446, https://doi.org/10.1016/j.carbpol.2016.10.017.

[33] L. Santamaría, M.A. Vicente, S.A. Korili, A. Gil, Progress in the removal of pharmaceutical compounds from aqueous solution using layered double hydroxides as adsorbents: a review, J. Environ. Chem. Eng. 8 (2020), 104577, https://doi.org/10.1016/j.jece.2020.104577.

[34] B. Paul, W. Chang, Mayenite-to-hydrocalumite transformation for the removal of chloride from salinized groundwater and the recycling potential of spent hydrocalumite for chromate removal, Desalination (2020), 114186, https://doi.org/10.1016/j.desal.2019.114186.

[35] C.F. Linares, J. Moscosso, V. Alzurutt, F. Ocanto, P. Bretto, G. González, Carbonated hydrocalumite synthesized by the microwave method as a possible antacid, Mater. Sci. Eng. C 61 (2016) 875–878, https://doi.org/10.1016/j.msec.2016.01.007.

[36] J. Granados-Reyes, P. Salagre, Y. Cesteros, G. Busca, E. Finocchio, Assessment through FT-IR of surface acidity and basicity of hydrocalumites by nitrile adsorption, Appl. Clay Sci. 180 (2019), 105180, https://doi.org/10.1016/j.clay.2019.105180.

[37] M. Rosset, O.W. Perez-Lopez, Cu–Ca–Al catalysts derived from hydrocalumite and their application to ethanol dehydrogenation, React. Kinet. Mech. Catal. 126 (2019) 497–511, https://doi.org/10.1007/s11144-018-1513-y.

[38] R.L. Souza Júnior, T.M. Rossi, C. Detoni, M.M.V.M. Souza, Glycerol carbonate production from transesterification of glycerol with diethyl carbonate catalyzed by Ca/Al-mixed oxides derived from hydrocalumite, Biomass. Convers. Biorefinery (2020), https://doi.org/10.1007/s13399-020-01110-4.

[39] B.R. Gevers, F.J.W.J. Labuschagné, Green synthesis of hydrocalumite (CaAl-OH-LDH) from Ca(OH)2 and Al(OH)3 and the parameters that influence its formation and speciation, Crystals 10 (2020) 672, https://doi.org/10.3390/cryst10080672.

[40] V. Matamoros, A. Duhec, J. Albaigés, J.M. Bayona, Photodegradation of carbamazepine, ibuprofen, ketoprofen and 17α-ethinylestradiol in fresh and seawater, Water Air. Soil Pollut. 196 (2009) 161–168, https://doi.org/10.1007/s11270-008-9765-1.

[41] J. Peuravuori, K. Pihlaja, Phototransformations of selected pharmaceuticals under low-energy UVA-vis and powerful UVB-UVA irradiations in aqueous solutions-the role of natural dissolved organic chromophoric material, Anal. Bioanal. Chem. 394 (2009) 1621–1636, https://doi.org/10.1007/s00216-009-2816-7.

[42] S. He, S. Zhang, J. Lu, Y. Zhao, J. Ma, M. Wei, D.G. Evans, X. Duan, Enhancement of visible light photocatalysis by grafting ZnO nanoplatelets with exposed (0001) facets onto a hierarchical substrate, Chem. Commun. 47 (2011) 10797–10799, https://doi.org/10.1039/c1cc14360c.

[43] H. Tian, Y. Fan, Y. Zhao, L. Liu, Elimination of ibuprofen and its relative photo-induced toxicity by mesoporous BiOBr under simulated solar light irradiation, RSC Adv. 4 (2014) 13061–13070, https://doi.org/10.1039/c3ra47304j.

[44] F.H. Li, K. Yao, W.Y. Lv, G.G. Liu, P. Chen, H.P. Huang, Y.P. Kang, Photodegradation of ibuprofen under UV–VIS irradiation: mechanism and toxicity of photolysis products, Bull. Environ. Contam. Toxicol. 94 (2015) 479–483, https://doi.org/10.1007/s00128-015-1494-8.

[45] R.B. Arthur, J.L. Bonin, L.P. Ardill, E.J. Rourk, H.H. Patterson, E.A. Stemmler, Photocatalytic degradation of ibuprofen over BiOCl nanosheets with identification of intermediates, J. Hazard. Mater. 358 (2018) 1–9, https://doi.org/10.1016/j.jhazmat.2018.06.018.

[46] M. Akkari, P. Aranda, C. Belver, J. Bedia, A. Ben Haj Amara, E. Ruiz-Hitzky, ZnO/sepiolite heterostructured materials for solar photocatalytic degradation of pharmaceuticals in wastewater, Appl. Clay Sci. 156 (2018) 104–109, https://doi.org/10.1016/j.clay.2018.01.021.

[47] Y. Gu, J. Yperman, R. Carleer, J. D'Haen, J. Maggen, S. Vanderheyden, K. Vanreppelen, R.M. Garcia, Adsorption and photocatalytic removal of Ibuprofen by activated carbon impregnated with TiO2 by UV–vis monitoring, Chemosphere 217 (2019) 724–731, https://doi.org/10.1016/j.chemosphere.2018.11.068.

[48] K. Patterson, K. Howlett, K. Patterson, B. Wang, L. Jiang, Photodegradation of ibuprofen and four other pharmaceutical pollutants on natural pigments sensitized TiO2 nanoparticles, Water Environ. Res. 92 (2020) 1152–1161, https://doi.org/10.1002/wer.1310.

[49] S. Chopra, D. Kumar, Ibuprofen as an emerging organic contaminant in environment, distribution and remediation, Heliyon 6 (2020), e04087, https://doi.org/10.1016/j.heliyon.2020.e04087.

[50] A.S. Sá, R.P. Feitosa, L. Honório, R. Peña-Garcia, L.C. Almeida, J.S. Dias, L.P. Brazuna, T.G. Tabuti, E.R. Triboni, J.A. Osajima, E.C. da Silva-Filho, A brief photocatalytic study of ZnO containing cerium towards ibuprofen degradation, Materials (Basel) 14 (2021) 5891, https://doi.org/10.3390/ma14195891.

[51] L. Wang, Z. Zhu, F. Wang, Y. Qi, W. Zhang, C. Wang, State-of-the-art and prospects of Zn-containing layered double hydroxides (Zn-LDH)-based materials for photocatalytic water remediation, Chemosphere 278 (2021) 130367, https://doi.org/10.1016/j.chemosphere.2021.130367.

[52] P. Bobde, R.K. Patel, R. Panchal, A. Sharma, A.K. Sharma, R.S. Dhodapkar, S. Pal, Utilization of layered double hydroxides (LDHs) and their derivatives as photocatalysts for degradation of organic pollutants, Environ. Sci. Pollut. Res. 28 (2021) 59551–59569, https://doi.org/10.1007/s11356-021-16296-x.

[53] N. Taoufik, M. Sadiq, M. Abdennouri, S. Qourzal, A. Khataee, M. Sillanpää, N. Barka, Recent advances in the synthesis and environmental catalytic applications of layered double hydroxides-based materials for degradation of emerging pollutants through advanced oxidation processes, Mater. Res. Bull. 154 (2022), 111924, https://doi.org/10.1016/j.materresbull.2022.111924.

[54] M. Olak-Kucharczyk, M. Foszpańczyk, R. Żyłła, S. Ledakowicz, Photodegradation and ozonation of ibuprofen derivatives in the water environment: Kinetics approach and assessment of mineralization and biodegradability, Chemosphere 291 (2022), 132742, https://doi.org/10.1016/j.chemosphere.2021.132742.

[55] S.N. Oba, J.O. Ighalo, C.O. Aniagor, C.A. Igwegbe, Removal of ibuprofen from aqueous media by adsorption: a comprehensive review, Sci. Total Environ. 780 (2021), 146608, https://doi.org/10.1016/j.scitotenv.2021.146608.

[56] F. Li, Q. Kong, P. Chen, M. Chen, G. Liu, W. Lv, K. Yao, Effect of halide ions on the photodegradation of ibuprofen in aqueous environments, Chemosphere 166 (2017) 412–417, https://doi.org/10.1016/j.chemosphere.2016.09.108.

[57] J.C.C. da Silva, J.A.R. Teodoro, R.J.d.C.F. Afonso, S.F. Aquino, R. Augusti, Photolysis and photocatalysis of ibuprofen in aqueous medium: Characterization of by-products via liquid chromatography coupled to high-resolution mass

spectrometry and assessment of their toxicities against Artemia salina, J. Mass Spectrom. 49 (2014) 145–153, https://doi.org/10.1002/jms.3320.

[58] R. Trujillano, V. Rives, I. García, Photocatalytic degradation of paracetamol in aqueous medium using TiO_2 prepared by the sol–gel method, Molecules 27 (2022) 2904, https://doi.org/10.3390/molecules27092904.

[59] R. Trujillano, C. Nájera, V. Rives, Activity in the photodegradation of 4-nitro-phenol of a Zn,Al hydrotalcite-like solid and the derived alumina-supported ZnO, Catalysts 10 (2020) 702, https://doi.org/10.3390/catl10060702.

[60] C. Bojer, J. Schöbel, T. Martin, M. Ertl, H. Schmalz, J. Breu, Clinical wastewater treatment: photochemical removal of an anionic antibiotic (ciprofloxacin) by mesostructured high aspect ratio ZnO nanotubes, Appl. Catal. B Environ. 204 (2017) 561–565, https://doi.org/10.1016/j.apcatb.2016.12.003.

[61] A. Kudo, Y. Miseki, Heterogeneous photocatalyst materials for water splitting, Chem. Soc. Rev. 38 (2009) 253–278, https://doi.org/10.1039/b800489g.

[62] M. Sánchez-Cantú, C. Barcelos-Santiago, C.M. Gomez, E. Ramos-Ramírez, M.D. L. Ruiz Peralta, N. Tepale, V.J. González-Coronel, A. Mantilla, F. Tzompantzi, Evaluation of hydrocalumite-like compounds as catalyst precursors in the photodegradation of 2,4-dichlorophenoxyacetic acid, Int. J. Photo 2016 (2016) 5256941, https://doi.org/10.1155/2016/5256941.

[63] C. Phrompet, C. Sriwong, P. Srepusharawoot, S. Maensiri, P. Chindaprasirt, C. Ruttanapun, Effect of free oxygen radical anions and free electrons in a $Ca12Al14O33$ cement structure on its optical, electronic and antibacterial properties, Heliyon 5 (2019), e01808, https://doi.org/10.1016/j.heliyon.2019.e01808.

[64] A.S. Darwish, D.I. Osman, H.A. Mohammed, S.K. Attia, Cuttlefish bone biowaste for production of holey aragonitic sheets and mesoporous mayenite-embedded Ag2CO3 nanocomposite: towards design high-performance adsorbents and visible-light photocatalyst for detoxification of dyes wastewater and waste oil recove, J. Photochem. Photobiol. A Chem. 421 (2021), 113523, https://doi.org/10.1016/j.jphotochem.2021.113523.

[65] S. Song, D. Kim, H.M. Jang, B.C. Yeo, S.S. Han, C.S. Kim, J.F. Scott, β-CuGaO2 as a strong candidate material for efficient ferroelectric photovoltaics, Chem. Mater. 29 (2022) 7596–7603, https://doi.org/10.1021/acs.chemmater.7b03141.

[66] H. Lei, M. Wu, Y. Liu, F. Mo, J. Chen, S. Ji, Y. Zou, X. Dong, Built-in piezoelectric field improved photocatalytic performance of nanoflower-like Bi2WO6 using low-power white LEDs, Chin. Chem. Lett. 32 (2021) 2317–2321, https://doi.org/10.1016/j.cclet.2020.12.019.

[67] M.O. Miranda, W.E. Cabral Cavalcanti, F.F. Barbosa, J. Antonio De Sousa, F. Ivan Da Silva, S.B.C. Pergher, T.P. Braga, Photocatalytic degradation of ibuprofen using titanium oxide: Insights into the mechanism and preferential attack of radicals, RSC Adv. 11 (2021) 27720–27733, https://doi.org/10.1039/d1ra04340d.

[68] G. Di, Z. Zhu, H. Zhang, J. Zhu, H. Lu, W. Zhang, Y. Qiu, L. Zhu, S. Küppers, Simultaneous removal of several pharmaceuticals and arsenic on Zn-Fe mixed metal oxides: combination of photocatalysis and adsorption, Chem. Eng. J. 328 (2017) 141–151, https://doi.org/10.1016/j.cej.2017.06.112.

[69] J. Prince, F. Tzompantzi, G. Mendoza-Damián, F. Hernández-Beltrán, J. S. Valente, Photocatalytic degradation of phenol by semiconducting mixed oxides derived from Zn(Ga)Al layered double hydroxides, Appl. Catal. B Environ. 163 (2015) 352–360, https://doi.org/10.1016/j.apcatb.2014.08.019.

[70] A. Monzón, E. Romeo, C. Royo, R. Trujillano, F.M. Labajos, V. Rives, Use of hydrotalcites as catalytic precursors of multimetallic mixed oxides. application in the hydrogenation of acetylene, Appl. Catal. A Gen. 185 (1999) 53–63, https://doi.org/10.1016/S0926-860X(99)00101-5.

[71] G. Fan, F. Li, D.G. Evans, X. Duan, Catalytic applications of layered double hydroxides: recent advances and perspectives, Chem. Soc. Rev. 43 (2014) 7040–7066, https://doi.org/10.1039/c4cs00160e.

[72] J.D. Phillips, L.J. Vandeperre, Anion capture with calcium, aluminium and iron containing layered double hydroxides, J. Nucl. Mater. 416 (2011) 225–229, https://doi.org/10.1016/j.jnucmat.2010.11.101.

[73] Y. Lu, Z. Zhang, Y. Xu, Q. Liu, G. Qian, CaFeAl mixed oxide derived heterogeneous catalysts for transesterification of soybean oil to biodiesel, Bioresour. Technol. 190 (2015) 438–441, https://doi.org/10.1016/j.biortech.2015.02.046.

[74] S.J. Xia, F.X. Liu, Z.M. Ni, J.L. Xue, P.P. Qian, Layered double hydroxides as efficient photocatalysts for visible-light degradation of Rhodamine B, J. Colloid Interface Sci. 405 (2013) 195–200, https://doi.org/10.1016/j.jcis.2013.05.064.

[75] A. Mantilla, F. Tzompantzi, J.L. Fernández, J.A.I.D. Góngora, R. Gómez, Photodegradation of phenol and cresol in aqueous medium by using Zn/Al + Fe mixed oxides obtained from layered double hydroxides materials, Catal. Today 150 (2010) 353–357, https://doi.org/10.1016/j.cattod.2009.11.006.

[76] M. Noorjahan, V. Durga Kumari, M. Subrahmanyam, L. Panda, Immobilized Fe (III)-HY: an efficient and stable photo-Fenton catalyst, Appl. Catal. B Environ. 57 (2005) 291–298, https://doi.org/10.1016/j.apcatb.2004.11.006.

[77] R.M. Liou, S.H. Chen, M.Y. Hung, C.S. Hsu, J.Y. Lai, Fe (III) supported on resin as effective catalyst for the heterogeneous oxidation of phenol in aqueous solution, Chemosphere 59 (2005) 117–125, https://doi.org/10.1016/j.chemosphere.2004.09.080.

[78] C.N.C. Hitam, A.A. Jalil, A review on exploration of Fe2O3 photocatalyst towards degradation of dyes and organic contaminants, J. Environ. Manag. 258 (2020), 110050, https://doi.org/10.1016/j.jenvman.2019.110050.

[79] A. Jiménez, M.A. Vicente, V. Rives, Thermochimica Acta Thermal study of the hydrocalumite – katoite – calcite system 713 (2022).

[80] ICDD database, (2022).

[81] M. Thommes, K. Kaneko, A.V. Neimark, J.P. Olivier, F. Rodriguez-Reinoso, J. Rouquerol, K.S.W. Sing, Physisorption of gases, with special reference to the evaluation of surface area and pore size distribution (IUPAC technical report), Pure Appl. Chem. 87 (2015) 1051–1069, https://doi.org/10.1515/pac-2014-1117.

[82] S. Brunauer, P.H. Emmet, E. Teller, Adsorption of gases in multimolecular layers, J. Am. Chem. Soc. 60 (1938) 309–319, https://doi.org/10.1016/j.fuel.2016.10.086.

[83] G. Pickett, Modification of the Brunauer-Emmett-Teller theory of multimolecular adsorption, J. Am. Chem. Soc. 67 (1958) 1958–1962, https://doi.org/10.1021/ja01227a027.

[84] L.G. Joyner, E.P. Barrett, P. Halenda, The determination of pore volume and area distributions in porous substances. I, 373–30, Comput. Nitrogen Isotherms, J. Am. Chem. Soc. 73 (1951), https://doi.org/10.1021/ja01151a046.

[85] D.R. Lide, CRC Handbook of Chemistry and Physics, 76th ed., Boca Raton, 1995.

[86] F. Cavani, F. Trifirò, A. Vaccari, Hydrotalcite-type anionic clays: preparation, properties and applications, Catal. Today 11 (1991) 173–301, https://doi.org/10.1007/BF03263563.

[87] A.V. Kapishnikov, R.M. Kenzhin, A.P. Koskin, A.M. Volodin, P.V. Geydt, Mayenite synthesis from hydroxide precursors: structure formation and active sites on its surface, Mater. (Basel) 15 (2022), https://doi.org/10.3390/ma15030778.

[88] A. Eisinas, K. Ruginyte, K. Baltakys, S. Demcak, T. Dambrauskas, M. Balintova, N. Stevulova, Cu^{2+} ion adsorption by synthetic mayenite and its thermal stability, Ceram. Int. 46 (2020) 29429–29435, https://doi.org/10.1016/j.ceramint.2020.05.028.

[89] H. Yi, Y. Lv, Y. Wang, X. Fang, V. Mattick, J. Xu, Ga-doped $Ca_{12}Al_{14}O_{33}$ mayenite oxide ion conductors: synthesis, defects, and electrical properties, RSC Adv. 9 (2019) 3809–3815, https://doi.org/10.1039/c8ra08254e.

[90] C. Li, D. Hirabayashi, K. Suzuki, Synthesis of higher surface area mayenite by hydrothermal method, Mater. Res. Bull. 46 (2011) 1307–1310, https://doi.org/10.1016/j.materresbull.2011.03.023.

[91] T. Dong, J. Li, F. Huang, L. Wang, J. Tu, Y. Torimoto, M. Sadakata, Q. Li, One-step synthesis of phenol by O⁻ and OH⁻ emission material, Chem. Commun. 1 (2005) 2724–2726, https://doi.org/10.1039/b419206k.

[92] J.M. Silva, R. Trujillano, V. Rives, M.A. Soria, L.M. Madeira, High temperature CO_2 sorption over modified hydrotalcites, Chem. Eng. J. 325 (2017) 25–34, https://doi.org/10.1016/j.cej.2017.05.032.

[93] X. Pan, J. Liu, S. Wu, H. Yu, Formation behavior of tricalcium aluminate hexahydrate in synthetic sodium aluminate solution with high alkali concentration and caustic ratio, Hydrometallurgy 195 (2020), 105373, https://doi.org/10.1016/j.hydromet.2020.105373.

[94] G.P. Wheeler, K.S. Choi, Investigation of p-type $Ca_2Fe_2O_5$ as a photocathode for use in a water splitting photoelectrochemical cell, ACS Appl. Energy Mater. 1 (2018) 4917–4923, https://doi.org/10.1021/acsaem.8b00934.

[95] X. Xu, S. Li, X. Wang, Y. Ma, X. Wang, K. Gao, Fabrication and characterization of $Ca_2Fe_2O_5$ nanofibers photocatalyst by sol-gel assisted electrospinning at low-temperature, Mater. Lett. 143 (2015) 75–79, https://doi.org/10.1016/j.matlet.2014.12.065.

[96] M. Padilla Villavicencio, A. Escobedo Morales, M. de, L. Ruiz Peralta, M. Sánchez-Cantú, L. Rojas Blanco, E. Chigo Anota, J.H. Camacho García, F. Tzompantzi, Ibuprofen photodegradation by Ag2O and Ag/Ag2O composites under simulated visible light irradiation, Catal. Lett. 150 (2020) 2385–2399, https://doi.org/10.1007/s10562-020-03139-6.

[97] G. Caviglioli, P. Valeria, P. Brunella, C. Sergio, A. Attilia, B. Gaetano, Identification of degradation products of Ibuprofen arising from oxidative and thermal treatments, J. Pharm. Biomed. Anal. 30 (2002) 499–509, https://doi.org/10.1016/S0731-7085(02)00400-4.

[98] A. Jakimska, M. Śliwka-Kaszyńska, J. Reszczyńska, J. Namieśnik, A. Kot-Wasik, Elucidation of transformation pathway of ketoprofen, ibuprofen, and furosemide in surface water and their occurrence in the aqueous environment using UHPLC-QTOF-MS, Anal. Bioanal. Chem. 406 (2014) 3667–3680, https://doi.org/10.1007/s00216-014-7614-1.

[99] S.H. Liu, W.T. Tang, P.H. Chou, Microwave-assisted synthesis of triple 2D g-C₃N₄/Bi₂WO₆/rGO composites for ibuprofen photodegradation: Kinetics, mechanism and toxicity evaluation of degradation products, Chem. Eng. J. 387 (2020), 124098, https://doi.org/10.1016/j.cej.2020.124098.

[100] T. Kwon, T.H. Pinnavaia, Pillaring of a layered double hydroxide by polyoxometalates with Keggin-ion structures, Chem. Mater. 1 (1989) 381–383.

[101] K. Chibwe, W. Jones, Intercalation of organic and inorganic anions into layered double hydroxides, J. Chem. Soc. Chem. Commun. (1989) 926–927.

[102] J. Tian, Q. Guo, Thermal decomposition of hydrocalumite over a temperature range of 400–1500 °C and its structure reconstruction in water, J. Chem. (2014) (2014), https://doi.org/10.1155/2014/454098.

[103] M. Rajamathi, G.D. Nataraja, S. Ananthamurthy, P. Vishnu Kamath, Reversible thermal behavior of the layered double hydroxide of Mg with Al: mechanistic studies, J. Mater. Chem. 10 (2000) 2754–2757, https://doi.org/10.1039/b006610i.

[104] J.A. van Bokhoven, J.C.A.A. Roelofs, K.P. de Jong, D.C. Koningsberger, Unique structural properties of the Mg–Al hydrotalcite solid base catalyst: an in situ study using Mg and Al K-Edge XAFS during calcination and rehydration, Chemistry (Easton) 7 (2001) 1258–1265, https://doi.org/10.1002/1521-3765(20010316)7:6<1258::aid-chem1258>3.3.co;2-9.